Forschung im Ingenieurwesen (2025)89:74
https://doi.org/10.1007/s10010-025-00842-x

ORIGINALARBEITEN/ORIGINALS

# Investigation of critical operating ranges in the rotor dynamics of axial flux machines using fourier methods

**Philipp Altoé[1] · Ulrich J. Römer[2] · Alexander Fidlin[1]**

Received: 19 June 2024 / Accepted: 22 May 2025
© The Author(s) 2025

**Abstract**

Rotors in electric drives are subject to external vibration excitation, particularly in mobile applications. In addition to fluctuations in the load torque, further axial and radial loads generally act on the rotor of an electrical machine. In combination with the electromagnetic forces inside the machine, these external loads can lead to large vibration amplitudes. In the present work, an axial flux machine in the type of a switched reluctance machine is investigated. The rotor dynamics are modeled in a minimal model by a rigid disk, which can tilt elastically around two axes in a spherical joint coupled to the shaft and rotates around the axis of symmetry at the motor speed. Under the influence of external excitation and electromagnetic forces in the air gap, the numerical results show critical operating ranges with high vibration amplitudes of the rotor disk.

**Zusammenfassung**

Rotoren in elektrischen Antrieben unterliegen insbesondere im Bereich mobiler Anwendungen einer externen Schwingungsanregung. Neben Schwankungen des Lastmoments wirken im Allgemeinen zusätzliche axiale und radiale Lasten auf den Rotor einer elektrischen Maschine. Diese äußeren Lasten können in Kombination mit den elektromagnetischen Kräften im Inneren der Maschine zu großen Schwingungsamplituden führen.

In der vorliegenden Arbeit wird eine Axialflussmaschine in der Bauform einer geschalteten Reluktanzmaschine untersucht. Die Rotordynamik wird in einem Minimalmodell durch eine starre Scheibe modelliert, welche in einem Kugelgelenk elastisch an die Welle angekoppelt um zwei Achsen kippen kann und mit der Motordrehzahl um die Symmetrieachse rotiert. Unter dem Einfluss der externen Anregung und der elektromagnetischen Kräfte im Luftspalt zeigen die numerischen Ergebnisse kritische Betriebsbereiche mit hohen Schwingungsamplituden der Rotorscheibe.

## 1 Introduction

The current trend towards electrified drivetrains requires developing new electric machines designed to meet the wide range of different drive concepts. The currently predominant radial flux machine design has been continuously improved in recent decades to meet new efficiency standards [14]. Other criteria, such as high power density, a good performance-to-cost ratio, and a robust design, are increasingly coming into focus, particularly with regard to mobile applications [6, 13]. Therefore, many other motor topologies were proposed and investigated. Among them, axial flux machines are receiving growing attention. Based on general sizing equations, the torque of an axial flux machine scales cubically with the rotor diameter, in contrast to the quadratic scaling observed in radial flux machines. This assessment implies the potential for higher torque and power density within a given axial length [11, 12, 22]. Numerous

✉ Philipp Altoé
philipp.altoe@kit.edu

Ulrich J. Römer
ulrich.roemer@imfd.tu-freiberg.de

Alexander Fidlin
alexander.fidlin@kit.edu

[1] Institut für Technische Mechanik, Teilinstitut Dynamik/Mechatronik, Karlsruher Institut für Technologie, 76131 Karlsruhe, Germany

[2] Institut für Mechanik und Fluiddynamik, TU Bergakademie Freiberg, 09599 Freiberg, Germany

Published online: 23 June 2025

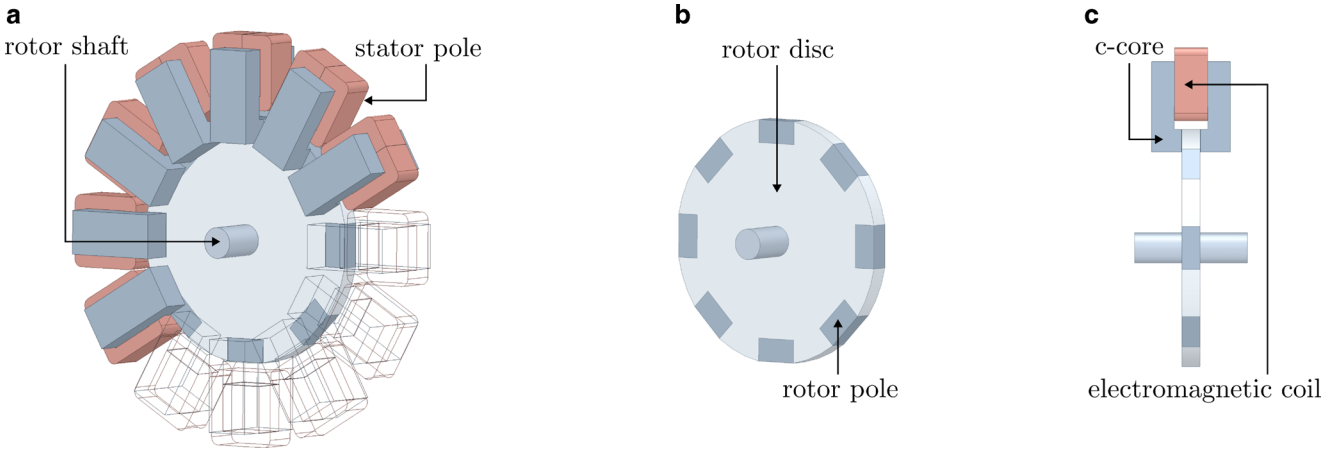


**Fig. 1** Topology of the investigated axial flux switched reluctance machine: **a** stator (partially transparent) and rotor, **b** rotor with ferromagnetic rotor poles, **c** side view with single stator pole

studies compare radial and axial flux machines [2, 7, 21, 27]. No universally valid conclusion favoring one topology over the other can be drawn, as these performance comparisons heavily depend on specific boundary conditions and mechanical design choices. Nonetheless, it can be concluded that axial flux machines offer advantages over radial flux machines in low-speed ranges and limited axial installation space. These characteristics make them well-suited for use in wheel hub drives and hybrid powertrains [24]. The compact axial dimension of axial flux machines arises from their disk-like rotor geometry. However, this geometry also results in a mechanically compliant structure more susceptible to deformation under the influence of high axial electromagnetic forces. This poses challenges not only in mechanical design to ensure structural integrity [24, 28] but also in NVH-behaviour because vibration excitation of the disk-shaped structure can lead to high sound radiation [20]. Therefore, the investigation of rotor dynamics is of particular interest for this type of machine.

The design of an axial flux switched reluctance machine considered in this work promises a robust, fault-tolerant design at low cost, as no rare earths are required for permanent magnets and there are no windings at the rotor [26]. However, improving NVH behavior is still important in current research for all types of reluctance machines [18, 23]. Previous rotordynamic studies on radial and axial flux machines focused on the internal excitation caused by unbalance magnetic pull. The external excitations that occur especially in mobile applications were mostly ignored and will be discussed in this paper which is an extension of the work presented in [1]. The paper is organized as follows:

Section 2 describes the design of an axial flux switched reluctance machine. The associated minimal model is presented in Sect. 3. The procedure for analyzing the electromagnetic forces should be transferable to other axial flux machines with a disk-shaped rotor and not be limited to the selected machine type. Section 4 shows the numerical methods used to analyze stationary solutions of the rotor dynamics based on Fourier methods and numerical solution continuation. The numerical results on the vibration behavior of the rotor disk under external and internal excitation and the discussion of critical operating ranges are given in Sect. 5. Section 6 summarizes the main results.

## 2 Axial flux switched reluctance machine

The type of machine investigated in this publication was proposed by Labak [17] and is shown in Fig. 1. The parameters used later are based on the design of a prototype from the Venus motor project funded by the European Union [9].

The rotor of the axial flux switched reluctance machine consists of a paramagnetic rotor disk with $n_r = 8$ ferromagnetic rotor poles attached to its circumference. The stator consists of $n_s = 12$ stator poles, which are positioned along the circumference of the rotor disk. Each stator pole has a ferromagnetic iron core in the shape of a c (c-core), which is wound by an electromagnetic coil and surrounds the rotor disk. Reluctant forces act on the rotor poles when a current $\boldsymbol{I}$ is applied to the coils. If the excitation currents are controlled properly, these forces lead to a resultant torque and drive the rotor.

## 3 Modeling approach

The modeling shown here focuses on a simple model that represents the primary interaction between structural parameters of the rotor disk under the influence of electromagnetic forces and an axial external excitation. The axial excitation appears to be the most relevant external excitation, as it causes a change in the air gap between the rotor

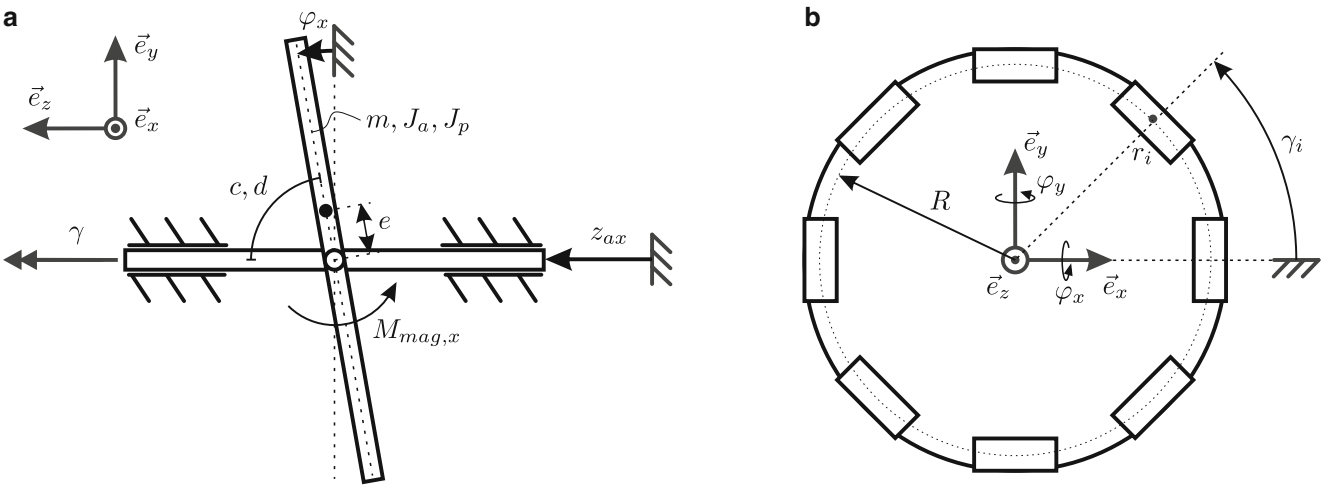


**Fig. 2** **a** Minimal model of mechanical subsystem, **b** position of one rotor pole $r_i$

and stator and thus directly influences the electromagnetic forces during operation.

### 3.1 Mechanical subsystem

The minimal model for the rotor of the machine shown in Fig. 2 is used to investigate the described relationships. It consists of a rigid rotor disk, which is elastically connected to the shaft in a spherical joint and can tilt around the $x$- and $y$-axis with the tilting angles $\varphi_x$ and $\varphi_y$. The rigid disk has the mass $m$, the axial mass moments of inertia $J_a$, the polar mass moment of inertia $J_p$ and the eccentricity $e$. The stiffness $c$ and the viscous damping $d$ should be selected so that the model represents the first two orthogonal vibration modes of the elastic rotor disk. For example, the stiffness and damping parameters can be determined from the discretization of a Kirchhoff plate using a Ritz ansatz, as shown in [10]. The model should thus enable a separate investigation of the first vibration modes in terms of modal reduction. However, an extension to further modes is easily possible in the future.

For the following investigations, a constant angular velocity $\dot{\gamma} = \Omega$ is assumed. The influence of the axial external excitation is considered via a given axial displacement $z_{ax}$ of the shaft. Linearized for small tilting angles $\varphi_x$ and $\varphi_y$, the following equations of motion result for the mechanical subsystem:

$$\begin{aligned} J_a\ddot{\varphi}_x + d\dot{\varphi}_x + J_p\dot{\gamma}\dot{\varphi}_y + c\varphi_x &= M_{\mathrm{mag},x} - me\ddot{z}_{ax}\sin(\gamma) \\ J_a\ddot{\varphi}_y + d\dot{\varphi}_y - J_p\dot{\gamma}\dot{\varphi}_x + c\varphi_y &= M_{\mathrm{mag},y} + me\ddot{z}_{ax}\cos(\gamma) \\ \dot{\gamma} &= \Omega = \mathrm{const.} \end{aligned} \quad (1)$$

The contained electromagnetic tilting torques $M_{\mathrm{mag},x}$ and $M_{\mathrm{mag},y}$ are discussed in the next subsection.

### 3.2 Electromagnetic subsystem

The next step in modeling deals with the electromagnetic forces acting on the rotor disk. These forces are determined by magneto-quasistatic calculations on a finite element model in the software *Ansys Maxwell*. In the magneto-quasistatic approximation of Maxwell's equations used, the calculated magnetic field and thus the electromagnetic forces depend only on the currents in the stator coils $\boldsymbol{I} = [I_1, \ldots, I_{n_s}]^T$ and the position of the rotor, which is given by the coordinates $\varphi_x, \varphi_y, \gamma$ and $z_{ax}$. Thus, a characteristic field of the electromagnetic forces $\boldsymbol{F}\left(\varphi_x, \varphi_y, \gamma, z_{ax}, \boldsymbol{I}\right)$ can be approximated by several finite element calculations.

The complexity of the finite element model needs to be reduced for the investigation as part of the minimal model. Due to the spatial separation of the rotor poles in the topology under consideration, it is assumed that the forces acting on one rotor pole are only slightly dependent on the position of adjacent rotor poles. Furthermore, the rotor poles are represented by a point due to their small expansion. As a result, the characteristic field $\boldsymbol{F}_i\left(\gamma_i, z_i, \boldsymbol{I}\right)$ of the forces acting on one rotor pole $i$ can be calculated only as a function of its angular position $\gamma_i$, the axial deflection $z_i$ and the current excitation $\boldsymbol{I}$ in the stator. The resulting electromagnetic tilting torques acting on the whole rotor disk can be calculated by superimposing the torques arising from one rotor pole, where a small-angle approximation for $\varphi_x$ and $\varphi_y$ is used:

$$\begin{aligned} &\gamma_i = \gamma + i\frac{2\pi}{n_r}, \qquad i = 1, \ldots, n_r, \\ &z_i \approx R\sin(\gamma_i)\varphi_x - R\cos(\gamma_i)\varphi_y + z_{ax}\ , \\ &M_{x,i} = F_{i,z}R\sin(\gamma_i), \quad M_{y,i} = -F_{i,z}R\cos(\gamma_i)\ , \\ &M_{mag,x} = \sum_{i=1}^{n_r} M_{x,i}, \quad M_{mag,y} = \sum_{i=1}^{n_r} M_{y,i}\ . \end{aligned} \quad (2)$$

The assumptions described above enable to reduce the number of required finite element calculations, as only the forces on one pole need to be calculated depending on a smaller number of parameters. Substituting Eq. (2) into Eq. (1) results in the complete equations of motion for the mechanical minimal model, which still depends on the current excitation $\boldsymbol{I}$ in the stator. To determine the current excitation, the dynamics of the electrical subsystem must be considered, which depend on the current control used in the electrical circuit and the feedback of the mechanical system. In this publication, the first step is to consider a given current excitation, which corresponds to an ideal current control in which the controller compensates for the feedback of the mechanical subsystem and other influences.

### 3.3 Harmonic analysis of electromagnetic forces

In an idealized operating condition, the reference value for the current control of the individual stator coils has a periodic behavior in the rotor angle $\gamma$. Fig. 3 shows that in an idealized operating condition, a coil is always energized when a rotor pole is directly in front of it in the circumferential direction. This results in a force $F_{tan}$ acting in the circumferential direction, which pulls the rotor pole $r_i$ under consideration into alignment with the subsequent stator pole. The reference value for the current of the overlapping stator pole is then set to zero so that the rotor does not experience an opposing force as it continues its rotation [5]. Even if the block-shaped reference value and, in particular, the sudden change in current cannot be achieved in real operation, a current controller will set an approximately periodic behavior of the currents $I_j(\gamma)$ at a stationary operating point.

If this periodic current is assumed, the characteristic curve of the forces acting on the rotor will also behave periodically. For example, specifying a current excitation as in Fig. 3 results in the characteristic curve in Fig. 4a for the axial forces acting on the rotor pole, which are the relevant forces for the minimal model. The discontinuities result from the assumption of an idealized block-shaped current. With a different current excitation, the shape and in particular the influence of different harmonics of the force characteristic can be significantly influenced.

The periodic behavior in the angle $\gamma$ allows a harmonic analysis that provides access to the structure of the acting forces. The periodicity is represented by a Fourier series

$$F_{i,z} = \frac{c_0(z_i)}{2} + \sum_{k=1}^{H} \left[ s_k(z_i) \sin\left(k \frac{2\pi}{\lambda} \gamma_i\right) + c_k(z_i) \cos\left(k \frac{2\pi}{\lambda} \gamma_i\right) \right] \tag{3}$$

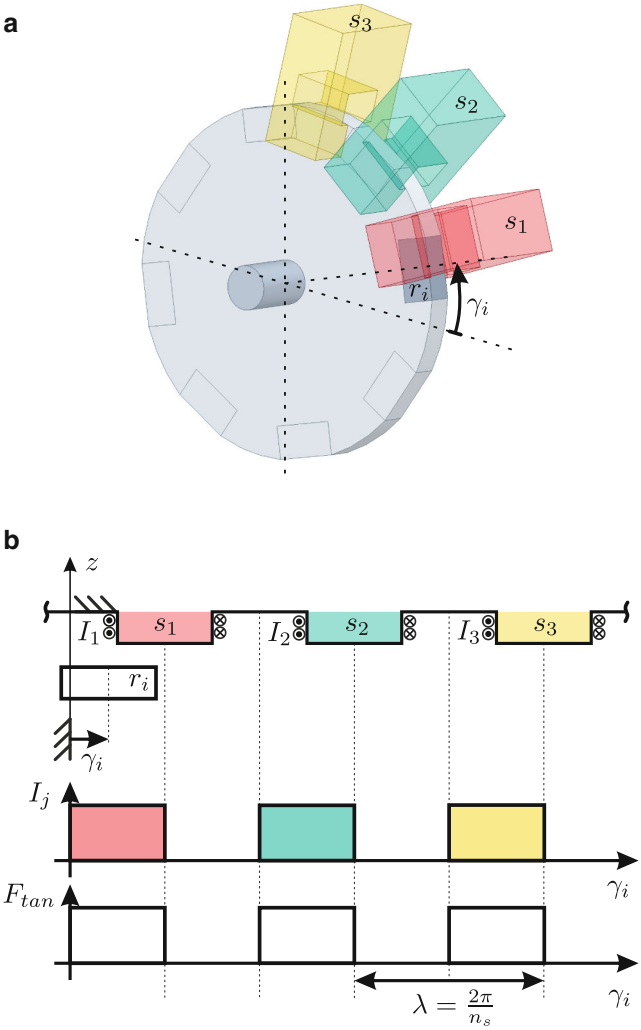


**Fig. 3** **a** Topology of the reluctance machine with exemplary labeling of different stator poles and one rotor pole, **b** developed view along the circumference and qualitative block-shaped reference value of the current excitation in the stator

with the wavelength $\lambda = \frac{2\pi}{n_s}$ and $H$ harmonics. Due to the non-constant behavior in the axial direction, the coefficients of the Fourier series $s_k$ and $c_k$ depend on the axial deflection of the rotor pole $z_i$. To describe this axial behavior, a cubic polynomial

$$F_{i,z}^{(m)}(z_i) = k_1^{(m)} z_i + k_3^{(m)} z_i^3, \qquad m = 0, \ldots, N-1 \tag{4}$$

is chosen as ansatz. The coefficients $k_1^{(m)}$ and $k_3^{(m)}$ are fitted to the characteristic curve at $N$ equidistant supporting sections

$$\gamma_i^{(m)} = \gamma_0 + m\Delta\gamma, \qquad \Delta\gamma = \frac{\lambda}{N} \tag{5}$$

over one period. Two exemplary supporting sections are shown in Fig. 4a.

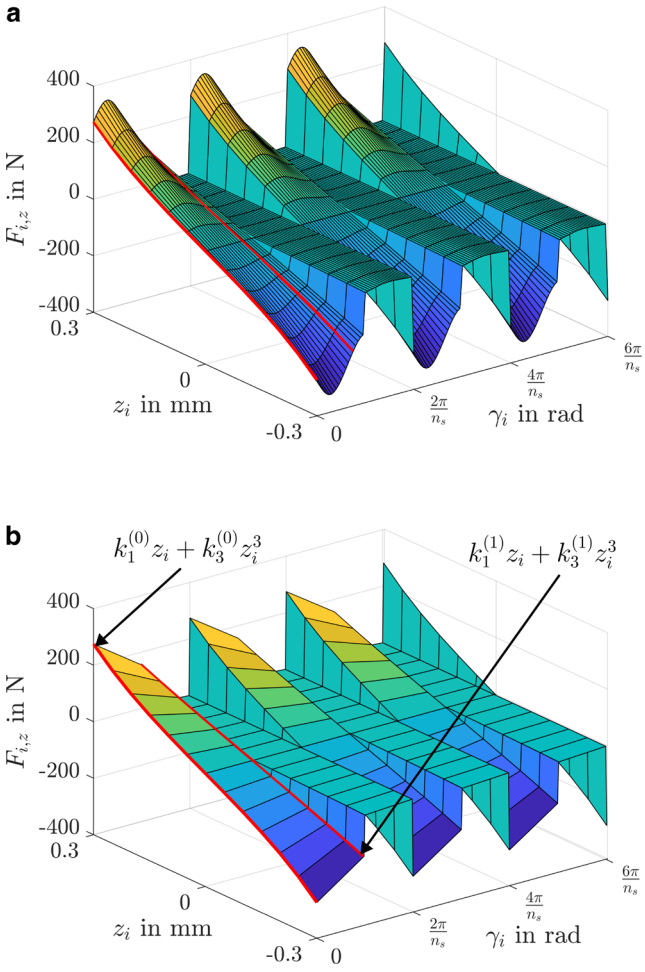


**Fig. 4** Characteristic curves of the forces acting axially on a rotor pole at a block-shaped current of 50 A and 22 windings: **a** Characteristic with $N$ supporting sections along $\gamma_i$, **b** linear interpolation in between two supporting sections

The coefficients of the Fourier series can subsequently be approximated using a discrete Fourier transform

$$c_k(z_i) = \frac{2}{\lambda} \sum_{m=0}^{N-1} F_{i,z}^{(m)} \cos\left(k \frac{2\pi}{\lambda} \gamma_i^{(m)}\right),$$
$$s_k(z_i) = \frac{2}{\lambda} \sum_{m=0}^{N-1} F_{i,z}^{(m)} \sin\left(k \frac{2\pi}{\lambda} \gamma_i^{(m)}\right) \tag{6}$$

and only depend on $z_i$. If an approach for interpolation between the different supporting sections is used, the exact coefficient integrals of the Fourier series can also be evaluated. Eq. (6) correspond to a linear interpolation between individual supporting sections along $\gamma_i$.

Using the procedure described, a general periodic characteristic curve of the axial forces can be approximated as a function of the coefficients $k_1^{(m)}$ and $k_3^{(m)}$. However, for interpreting the results in the following section, a simplified consideration is useful to clarify the influence of the non-linear terms in the axial direction. For this purpose, only two supporting sections within a period are selected, as shown in Fig. 4b. In the range $\gamma_i \in \left[0, \frac{\pi}{n_s}\right]$, the characteristic curve is linearly interpolated along $\gamma_i$ and set to zero in the following range $\gamma_i \in \left(\frac{\pi}{n_s}, \frac{2\pi}{n_s}\right)$ corresponding to an excitation with the idealized block-shaped current. After evaluating the coefficient integrals, this results in a closed form representation of the Fourier coefficients as a function of the parameters $k_1^{(0)}$, $k_3^{(0)}$, $k_1^{(1)}$ and $k_3^{(1)}$ at both supporting sections:

$$c_0 = \frac{\left(k_1^{(0)} + k_1^{(1)}\right) z_i + \left(k_3^{(0)} + k_3^{(1)}\right) z_i^3}{4},$$
$$c_k = \frac{1-(-1)^k}{\pi^2 k^2} \left[\left(k_1^{(0)} - k_1^{(1)}\right) z_i + \left(k_3^{(0)} - k_3^{(1)}\right) z_i^3\right], \tag{7}$$
$$s_k = \frac{\left(k_1^{(0)} - (-1)^k\, k_1^{(1)}\right) z_i + \left(k_3^{(0)} - (-1)^k\, k_3^{(1)}\right) z_i^3}{\pi k}.$$

For the topology considered in the results section with $n_s = 12$ stator poles and $n_r = 8$ rotor poles, a closed-form representation for the linear terms of the electromagnetic tilting torques can also be given by evaluating Eq. (2):

$$M_{mag,x} = c_{\text{mag}} \varphi_x + \mathcal{O}\left(\varphi_{x,y}^3\right), \tag{8}$$

$$M_{mag,y} = c_{\text{mag}} \varphi_y + \mathcal{O}\left(\varphi_{x,y}^3\right), \tag{9}$$

with

$$c_{\text{mag}} = R^2 \left(k_1^{(0)} + k_1^{(1)} + 3\left(k_3^{(0)} + k_3^{(1)}\right) z_{ax}^2\right) + \frac{R^2 \left(k_1^{(0)} - k_1^{(1)} + 3\left(k_3^{(0)} - k_3^{(1)}\right) z_{ax}^2\right)}{2\pi} \sum_{k=1}^{\infty} \frac{4}{k} \sin(2k n_s \gamma). \tag{10}$$

After insertion into the equations of motion (1), it can be seen that the electromagnetic tilting torques cause a negative, non-linear stiffness component and thus reduce the restoring force in the tilting of the rotor disk. Taking into account the constant angular velocity $\dot{\gamma} = \Omega$, a parametric excitation of the restoring force in the frequencies $2k n_s \Omega$ is apparent, which is additionally coupled with frequencies from the axial excitation $z_{ax}$.

## 4 Numerical methods

Due to external axial excitation in combination with parametric excitation, periodic or quasi-periodic stationary solutions of the rotor can be expected. Among numerical forward simulation, two different Fourier methods and numerical solution continuation are used to investigate these solutions. The Fourier methods are roughly described in this section, followed by a method for initializing the quasi-periodic solution branches, as this can generally cause problems. For a detailed explanation of the methods themselves, the interested reader is referred to [25] and [3], for example.

We consider the transformation of the equations of motion (1) to a first-order system

$$\begin{aligned} \dot{\boldsymbol{x}} &= \boldsymbol{f}(\boldsymbol{x}, \Omega t), \quad \boldsymbol{x} \in \mathbb{R}^N, \\ & \boldsymbol{f}(\boldsymbol{x}, \Omega t) = \boldsymbol{f}(\boldsymbol{x}, \Omega t + 2\pi) \end{aligned} \tag{11}$$

with state vector $\boldsymbol{x} = [\varphi_x, \dot{\varphi_x}, \varphi_y, \dot{\varphi_y}]^T$ and $N = 4$ where the right-hand-side $\boldsymbol{f}$ is $2\pi$-periodic in $\Omega t$. For simplicity, the case of a quasi-periodic solution $\boldsymbol{x}^*(t)$ of Eq. (11) with only two incommensurable base frequencies $\Omega$ and $\omega$ is considered, where $\omega$ describes an apriori unknown autonomous base-frequency. Such a solution can generally be described by a torus function $\boldsymbol{Z}(\theta_1, \theta_2) : \mathbb{T}^2 \to \mathbb{R}^4$, where the torus coordinates $\theta_1$ and $\theta_2$ are defined as a function of the incommensurable base frequencies:

$$\boldsymbol{x}^*(t) = \boldsymbol{Z}(\theta_1(t), \theta_2(t)) = \boldsymbol{Z}(\Omega t, \omega t). \tag{12}$$

Since, for an incommensurable frequency base, the torus is filled densely in time, one can restrict oneself to the determination of the torus function instead of the actual quasi-periodic solution evolving on it. By introducing the torus coordinates as hyper-time variables, the time derivative can be transformed to

$$\frac{\mathrm{d}(\cdot)}{\mathrm{d}t} = \frac{\partial(\cdot)}{\partial\theta_1}\Omega + \frac{\partial(\cdot)}{\partial\theta_2}\omega. \tag{13}$$

Inserted into Eq. (11), the result is the so-called *invariance equation*, which describes, in combination with periodic boundary conditions the torus function as a partial differential equation:

$$\begin{aligned} &\frac{\partial \boldsymbol{Z}}{\partial\theta_1}\Omega + \frac{\partial \boldsymbol{Z}}{\partial\theta_2}\omega = \boldsymbol{f}(\boldsymbol{Z}, \theta_1) \\ &\boldsymbol{Z}(\theta_1, \theta_2) = \boldsymbol{Z}(\theta_1 + 2\pi, \theta_2) \\ &\boldsymbol{Z}(\theta_1, \theta_2) = \boldsymbol{Z}(\theta_1, \theta_2 + 2\pi) \end{aligned} \tag{14}$$

There are several methods for solving it, two of which are used and shortly described below.

### 4.1 Semi-discretization: Spectral system

The first method is used in this paper in particular to simplify the initialization of the second method later on. Here, the ansatz

$$\begin{aligned} \boldsymbol{Z}_a^s = \boldsymbol{a}_0^s(\theta_2) \\ + \sum_{k=1}^{H_{\theta_1}} \left[\boldsymbol{a}_{c,k}^s(\theta_2)\cos(k\theta_1) + \boldsymbol{a}_{s,k}^s(\theta_2)\sin(k\theta_1)\right] \end{aligned} \tag{15}$$

is chosen to solve Eq. (14). The upper index $s$ is introduced to distinguish the semi-discretization method from the full discretization method with upper index $f$ described later. The ansatz (15) represents the periodicity in the first hyper-time $\theta_1$ by a Fourier series with the harmonic order $H_{\theta_1}$. However, the coefficients remain variable in the second hyper-time $\theta_2$ to allow for possible periodicities. Defining a residual function

$$\boldsymbol{r}(\boldsymbol{Z}_a) = \frac{\partial \boldsymbol{Z}_a}{\partial\theta_1}\Omega + \frac{\partial \boldsymbol{Z}_a}{\partial\theta_2}\omega - \boldsymbol{f}(\boldsymbol{Z}_a, \theta_1), \tag{16}$$

for Eq. (11), the residual $\boldsymbol{r}_a^s = \boldsymbol{r}(\boldsymbol{Z}_a^s)$ is projected by a Galerkin ansatz onto the ansatz-functions of Eq. (15):

$$\begin{aligned} &\frac{1}{2\pi}\int_0^{2\pi} 1 \cdot \boldsymbol{r}_a^s(\theta_1, \theta_2)\mathrm{d}\theta_1 = \boldsymbol{0} \\ &\frac{1}{2\pi}\int_0^{2\pi} \cos(k\theta_1) \cdot \boldsymbol{r}_a^s(\theta_1, \theta_2)\mathrm{d}\theta_1 = \boldsymbol{0}, \quad k = 1, \ldots, H_{\theta_1} \\ &\frac{1}{2\pi}\int_0^{2\pi} \sin(k\theta_1) \cdot \boldsymbol{r}_a^s(\theta_1, \theta_2)\mathrm{d}\theta_1 = \boldsymbol{0}, \quad k = 1, \ldots, H_{\theta_1} \end{aligned} \tag{17}$$

Sorting the resulting equations for the coefficients in a state-vector

$$\boldsymbol{Y} = \begin{bmatrix} \boldsymbol{a}_0^s(\theta_2) \\ \boldsymbol{a}_{c,1}^s(\theta_2) \\ \boldsymbol{a}_{s,1}^s(\theta_2) \\ \vdots \\ \boldsymbol{a}_{s,H_{\theta_1}}^s(\theta_2) \end{bmatrix}, \qquad \boldsymbol{Y} \in \mathbb{R}^{(2H_{\theta_1}+1)N} \tag{18}$$

and eliminating the apriori unknown frequency $\omega$ by insertion of the transformation $\theta_2 = \omega t$ yields the so-called spectral system

$$\overbrace{\begin{bmatrix} \frac{\mathrm{d}}{\mathrm{d}t}\boldsymbol{a}_0^s(\theta_2) \\ \frac{\mathrm{d}}{\mathrm{d}t}\boldsymbol{a}_{c,1}^s(\theta_2) \\ \frac{\mathrm{d}}{\mathrm{d}t}\boldsymbol{a}_{s,1}^s(\theta_2) \\ \vdots \end{bmatrix}}^{\frac{\mathrm{d}}{\mathrm{d}t}\boldsymbol{Y}} = \overbrace{-\Omega \begin{bmatrix} 0 \\ \boldsymbol{a}_{s,1}^s \\ -\boldsymbol{a}_{c,1}^s \\ \vdots \end{bmatrix} + \begin{bmatrix} \frac{1}{2\pi}\int_0^{2\pi} 1 \cdot \boldsymbol{f}(\boldsymbol{Z}_a^s, \theta_1)\mathrm{d}\theta_1 \\ \frac{1}{2\pi}\int_0^{2\pi} \cos(\theta_1) \cdot \boldsymbol{f}(\boldsymbol{Z}_a^s, \theta_1)\mathrm{d}\theta_1 \\ \frac{1}{2\pi}\int_0^{2\pi} \sin(\theta_1) \cdot \boldsymbol{f}(\boldsymbol{Z}_a^s, \theta_1)\mathrm{d}\theta_1 \\ \vdots \end{bmatrix}}^{\boldsymbol{f}^s(\boldsymbol{Y})} \tag{19}$$

as a system of $(2H_{\theta_1} + 1)\, N$ ordinary differential equations. Periodic solutions with period $T$ of this spectral system correspond to quasi-periodic solutions of the full system with $\omega = \frac{2\pi}{T}$. It should be noted that the spectral system can also be used to find periodic solutions of the full system since an equilibrium of the spectral system corresponds to the well-known equations in the harmonic balance method (see e.g. [15]).

### 4.2 Full discretization: Fourier-Galerkin method

In the second method, also the periodicity in $\theta_2$ is taken into account in the ansatz as a multi-dimensional Fourier series

$$\begin{aligned} \boldsymbol{Z}_a^f &= \boldsymbol{a}_0^f + \sum_{\boldsymbol{k}\in\mathcal{H}} \left[ \boldsymbol{a}_{c,\boldsymbol{k}}^f \cos(\boldsymbol{k}\cdot\boldsymbol{\theta_h}) + \boldsymbol{a}_{s,\boldsymbol{k}}^f \sin(\boldsymbol{k}\cdot\boldsymbol{\theta_h}) \right], \\ \boldsymbol{k} &= [k_{\theta_1}, k_{\theta_2}]^T, \boldsymbol{\theta_h} = [\theta_1, \theta_2]^T \end{aligned} \tag{20}$$

with multi-index $\boldsymbol{k}$ and vector of hyper-times $\boldsymbol{\theta}_h$. $\mathcal{H}$ is a finite set of 2-dimensional multi-indices and in this work, chosen as $\mathcal{H} = \{\{1, \ldots, H_{\theta_1}\} \times \{-H_{\theta_2}, \ldots, H_{\theta_2}\} \cup \{0\} \times \{1, \ldots, H_{\theta_2}\}\} \subset \mathbb{Z}^2$. As for the first method, the ansatz is inserted into the residual function $\boldsymbol{r}_a^f = \boldsymbol{r}(\boldsymbol{Z}_a^f)$ and a projection in the sense of Galerkin onto the multi-dimensional ansatz functions results in a system of $N_f = (2|\mathcal{H}| + 1)N$ purely algebraic equations

$$\begin{aligned} &\frac{1}{(2\pi)^2}\int_0^{2\pi}\int_0^{2\pi} \boldsymbol{r}_a^f \cdot 1 \mathrm{d}\theta_1 \mathrm{d}\theta_2 = \boldsymbol{0} \\ &\frac{2}{(2\pi)^2}\int_0^{2\pi}\int_0^{2\pi} \boldsymbol{r}_a^f \cdot \cos(\boldsymbol{k}\cdot\boldsymbol{\theta_h})\, \mathrm{d}\theta_1 \mathrm{d}\theta_2 = \boldsymbol{0}, \quad k \in \mathcal{H} \\ &\frac{2}{(2\pi)^2}\int_0^{2\pi}\int_0^{2\pi} \boldsymbol{r}_a^f \cdot \sin(\boldsymbol{k}\cdot\boldsymbol{\theta_h})\, \mathrm{d}\theta_1 \mathrm{d}\theta_2 = \boldsymbol{0}, \quad k \in \mathcal{H} \end{aligned} \tag{21}$$

which define the $N_f$ unknown coefficients in Eq. (20). Since the autonomous frequency $\omega$ is generally unknown, the system has $N_f + 1$ unknowns, and it can be extended by different phase conditions for a better-posed problem (see e.g. [3]).

### 4.3 Initialization procedure

The calculation of quasi-periodic solutions from the semi-discretization method is often slow compared to the full discretization method because one usually has to combine it with further time-domain-based methods to find periodic solutions, e.g. shooting methods. Furthermore, spurious bifurcations that are not present in the full system can arise. Also, the stability of solutions of the spectral system is not necessarily identical to the stability of the full system [19].

However, a useful application lies in the initialization of the full-discretization method when a Hopf bifurcation of the spectral system occurs. In this case, an equilibrium position of the spectral system is continued first, corresponding to a periodic solution of the full system. At a Hopf bifurcation point, an initial periodic solution of the spectral system can be determined tangentially to the central manifold, corresponding to a quasi-periodic solution of the full system. This procedure can be particularly advantageous for unstable quasi-periodic solutions, as an initial solution for the large number of unknowns and the apriori unknown autonomous frequency is generally difficult to find and can be obtained from the following procedure.

#### 4.3.1 Initial periodic solution of the spectral system at hopf point

One exemplary procedure to find an initial periodic solution in a hopf point with a non-vanishing first Lyapunov coefficient is described in [16]. For this purpose, the Jakobi matrix of the spectral system (19)

$$\boldsymbol{J}_H = \left.\frac{\partial \boldsymbol{f}^s(\boldsymbol{Y})}{\partial \boldsymbol{Y}}\right|_{\boldsymbol{Y}=\boldsymbol{Y}_H}, \tag{22}$$

evaluated at a hopf bifurcation point $\boldsymbol{Y}_H$ and the corresponding normalized critical eigenvectors $\boldsymbol{q}, \bar{\boldsymbol{q}}$ to the eigenvalues $i\omega_0$, $-i\omega_0$ are determined. An initial periodic solution $\boldsymbol{Y}^*$ with the autonomous frequency $\omega = \omega_0$ is then given by

$$\boldsymbol{Y}^*(t) = \boldsymbol{Y}_H + 2\varepsilon(\Re(\boldsymbol{q})\cos(\omega t) - \Im(\boldsymbol{q})\sin(\omega t)) \tag{23}$$

where $\varepsilon$ denotes a small constant.

#### 4.3.2 Multi-dimensional Fourier coefficients at Hopf point

To initialize the full discretization method from a periodic solution $\boldsymbol{Y}^*(t)$ with base frequency $\omega$ of the spectral system, the solution can generally be inserted into Eq. (15) under consideration of the inverse transformation $t = \frac{\theta_2}{\omega}$, yielding the approximate solution in state space as the torus function $\boldsymbol{Z}_a^{s^*}(\theta_1, \theta_2)$. The multi-dimensional Fourier coefficients in the ansatz of the full discretization method (20) are readily calculated by the multi-dimensional Fourier transform, yielding the following expressions:

$$\boldsymbol{a}_0^f = \frac{1}{2\pi}\int_0^{2\pi} 1 \cdot \boldsymbol{a}_0^{s^*}(\theta_2)\mathrm{d}\theta_2 \tag{24}$$

$$\boldsymbol{a}_{c,[0,k_{\theta_2}]^T}^f = \frac{1}{\pi}\int_0^{2\pi} \cos(k_{\theta_2}\theta_2) \cdot \boldsymbol{a}_0^{s^*}(\theta_2)\mathrm{d}\theta_2 \tag{25}$$

$$\boldsymbol{a}_{s,[0,k_{\theta_2}]^T}^f = \frac{1}{\pi}\int_0^{2\pi} \sin(k_{\theta_2}\theta_2) \cdot \boldsymbol{a}_0^{s^*}(\theta_2)\mathrm{d}\theta_2 \tag{26}$$

$$\begin{aligned}\boldsymbol{a}_{c,[k_{\theta_1},k_{\theta_2}]^T}^f = \frac{1}{2\pi}\Bigg[&\int_0^{2\pi} \cos(k_{\theta_2}\theta_2) \cdot \boldsymbol{a}_{c,k_{\theta_1}}^{s^*}(\theta_2)\mathrm{d}\theta_2 \\ &-\mathrm{sgn}(k_{\theta_2})\int_0^{2\pi} \sin(k_{\theta_2}\theta_2) \cdot \boldsymbol{a}_{s,k_{\theta_1}}^{s^*}(\theta_2)\mathrm{d}\theta_2\Bigg]\end{aligned} \tag{27}$$

$$\begin{aligned}\boldsymbol{a}_{s,[k_{\theta_1},k_{\theta_2}]^T}^f = \frac{1}{2\pi}\Bigg[&\int_0^{2\pi} \cos(k_{\theta_2}\theta_2) \cdot \boldsymbol{a}_{s,k_{\theta_1}}^{s^*}(\theta_2)\mathrm{d}\theta_2 \\ &+\mathrm{sgn}(k_{\theta_2})\int_0^{2\pi} \sin(k_{\theta_2}\theta_2) \cdot \boldsymbol{a}_{c,k_{\theta_1}}^{s^*}(\theta_2)\mathrm{d}\theta_2\Bigg]\end{aligned} \tag{28}$$

For the previously shown initialization at a Hopf point, it is known by Eq. (23) that the solution is only one-periodic in the autonomous frequency $\omega$ and the corresponding coefficients with $k_{\theta_2} \in \{-1, 0, 1\}$ in the hyper-index $\boldsymbol{k}$ should be sufficient. Furthermore, the Fourier-integrals in (24–28) can be directly replaced by the corresponding coefficients in (23).

## 5 Numerical results

The following standard structural parameters, which are based on the system in [9], are selected for the numerical evaluations:

$$\begin{aligned} c &= 1.2 \cdot 10^6\,\mathrm{Nm} & J_a &= 0.033665\,\mathrm{kgm}^2 \\ J_p &= 0.06683\,\mathrm{kgm}^2 & d &= 0.04\,\mathrm{Nms} \\ m &= 10\,\mathrm{kg} & R &= 145\,\mathrm{mm} \\ e &= 0.01\,\mathrm{mm} \end{aligned} \tag{29}$$

These correspond to a rotor disk with a natural frequency of $f = 950$ Hz and a damping ratio $D = 0.0001$ of the first vibration mode. For the external and electromagnetic excitation, the parameters

$$\begin{aligned} n_s &= 12 & n_r &= 8 \\ H &= 10 & N &= 20 \\ z_a &= 0.1\,\mathrm{mm} & I &= 50\,\mathrm{A} \end{aligned} \tag{30}$$

were selected. With these parameters, the finite element calculations yield the force characteristic shown in Fig. 4a.

The influence of different axial excitation frequencies on the system behavior is evaluated first by forward time simulation. For this purpose, several run-up simulations are carried out in which the axial excitation is given periodically by multiples of the rotor angular velocity $\Omega$:

$$z_{ax} = z_a \sin(k_{ax}\Omega t) \tag{31}$$

The result is shown in Fig. 5. The color scale corresponds to the maximum axial deflection at the edge of the rotor disk $R\sin\varphi_x$. Several areas with increased amplitudes are apparent, which can be interpreted using the equations of

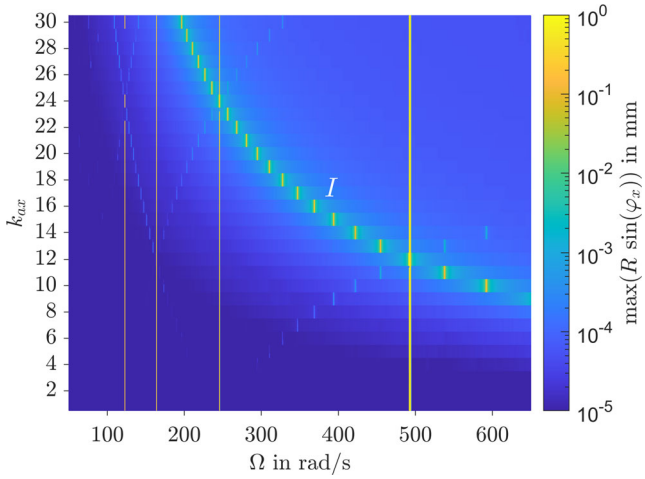


**Fig. 5** Maximum axial deflection on the rotor's circumference during run-up with axial excitation

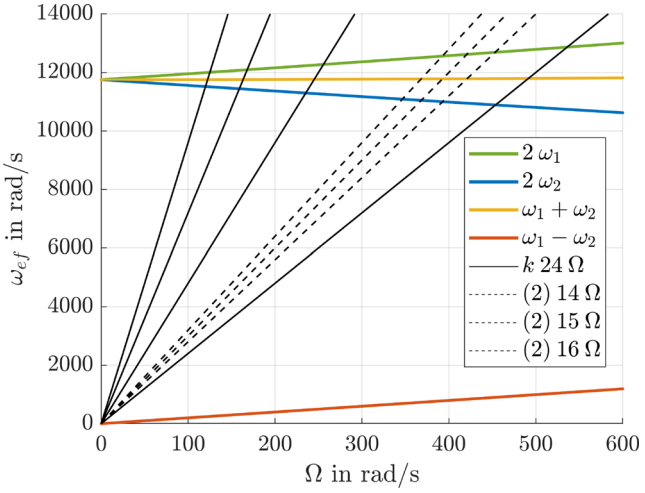


**Fig. 6** Modified Campbell-diagram

motion (1) and the structure of the electromagnetic tilting torques (10).

### 5.1 Fundamental parametric combination resonances

The vertical lines in Fig. 5, independent of the axial excitation frequency, correspond to regions where the conditions for a fundamental parametric resonance are fulfilled. In this case, the parametric excitation frequency must correspond to a double natural frequency or the sum or difference of two natural frequencies of the system. A modified Campbell diagram is proposed for interpretation, shown in Fig. 6. It depicts the double natural frequencies and the sum or difference of the two rotor's natural frequencies in forward whirl $\omega_1$ and backward whirl $\omega_2$.

The solid black lines correspond to the parametric excitation frequencies from the electromagnetic excitation (cf. Eq. (10)), and the intersections with other lines therefore represent potential areas of parametric resonance or anti-resonance. In Fig. 5, however, only the fundamental parametric sum-combination resonances up to $k = 4$ with increased amplitudes are apparent for the system under consideration:

$$2k\,n_s\Omega = \omega_1 + \omega_2, \qquad k = 1, \ldots, 4. \tag{32}$$

The influence of higher multiples disappears as the amplitude of the parametric excitation in Eq. (10) decreases with increasing $k$.

### 5.2 Resonance due to axial excitation

The line marked with $I$ in Fig. 5 is in particular due to resonance from the axial excitation in Eq. (1), where the condition

$$(k_{ax} \pm 1)\,\Omega = \omega_i \tag{33}$$

is fulfilled. In addition, the fundamental parametric combination resonance from the frequencies of the axial excitation in Eq. (10) corresponds to this range and is given by the following condition:

$$2k_{ax}\Omega = \omega_1 + \omega_2\ . \tag{34}$$

For the case $k_{ax} = 15$, these conditions are shown in Fig. 6 with dashed black lines. The increased amplitudes correspond to the resonance in rotor's forward whirl $(k_{ax} + 1)\,\Omega = \omega_1$, the resonance in backward whirl $(k_{ax} - 1)\,\Omega = \omega_2$ and the parametric combination resonance $2k_{ax}\Omega = \omega_1 + \omega_2$.

### 5.3 Fundamental parametric combination resonances from the coupling of excitations

The remaining lines with slightly increased amplitudes appear in areas of parametric resonance with a parametric excitation frequency, which is due to a multiplicative coupling of the axial and electromagnetic excitation in the second term of Eq. (10). In these areas, the condition of parametric sum-combination resonance is fulfilled again:

$$2k\,n_s\Omega \pm 2k_{ax}\Omega = \omega_1 + \omega_2. \tag{35}$$

As $k$ increases, the amplitude of the resulting disk oscillation decreases.

### 5.4 Further investigation using Fourier methods

In this subsection, results are shown for the particular case $k_{ax} = 11$ in the ranges of the pure fundamental combination resonance $\Omega \in [480, 495]$ rad/s and the resonance from axial excitation $\Omega \in [537, 539]$ rad/s using the Fourier methods shown in Sect. 4.

Periodic solutions are initialized by time simulation of the full system and afterward continued as equilibrium solution of the spectral system in (19) using the software *MatCont* [8]. Quasi-periodic solutions are initialized by the procedure described in Sect. 4.3.1 and continued with the full discretization method. The algebraic equation system is continued by the arc-length continuation scheme implemented in the software *NLvib* [15]. The numbers of harmonics $H_{\theta_1} = 14$ and $H_{\theta_2} = 1$ are chosen. A stroboscopic

map, which can also be understood as a Poincaré map, is selected for comparison. For each angular velocity, starting from a steady state, $m$ points are plotted at a time interval of $\Delta t = \frac{2\pi}{\Omega}$. The stroboscopic map is always started at a point of maximum amplitude of the rotor disk.

The two small peaks of the periodic solution in Fig. 7a correspond to the system's resonance in the natural frequency of the rotor's forward whirl on the left and backward whirl on the right. They show a left-bended backbone behavior, which is due to the softening behavior of the non-linear electromagnetic forces. The periodic solution loses its stability between the two peaks due to the parametric combination resonance in Eq. (34) and quasi-periodic solutions arise. The quasi-periodic solution branches emerge from two Neimarck-Sacker bifurcations, corresponding to Hopf-bifurcations in the spectral system. Stability of the quasi-periodic solution obtained with the full discretization method was not assessed yet and, hence, it is not shown in the figure. However, time simulation and the following stroboscopic maps initialized from the approximate solutions indicate a predominantly stable upper and an unstable lower solution branch. Fig. 7b and c show stroboscopic maps for a run-up and run-down time simulation. There, the periodic and quasi-periodic behavior can also be distinguished. In the periodic range, the points are mapped onto themselves, and in the quasi-periodic range, they would densely fill the vertical line segments with an increasing number of maps $m$. The time simulations indicate an unstable area of the upper quasi-periodic solution branch in the area around $\Omega \approx 537,5$ rad/s since a fall down to the periodic solution occurs during run-up and run-down. Although no method has yet been implemented to evaluate the stability and further bifurcations on the quasi-periodic solution branches, this illustrates the usefulness of semi-analytical methods for solution continuation. Through pure time simulation, the again stable quasi-periodic solution branch and initialization point of Fig. 7b could only be found through a large number of time simulations with varied initial conditions.

The investigation of the range $\Omega \in [480, 495]$ rad/s in Fig. 8 shows a similar non-linear system behavior. Due to the parametric combination resonance, the periodic solution with vanishingly low amplitude loses stability. However, the amplitude of the resulting quasi-periodic solution is limited. Due to the softening behavior, the system's natural frequencies decrease with increasing amplitude, and the condition of the parametric combination resonance can still be fulfilled during the run-down. Therefore, the run-down seems more critical for the system shown, as the system remains on the solution branch of the quasi-periodic solution with higher amplitudes. During run-up without any perturbation, the system remains on the periodic solution

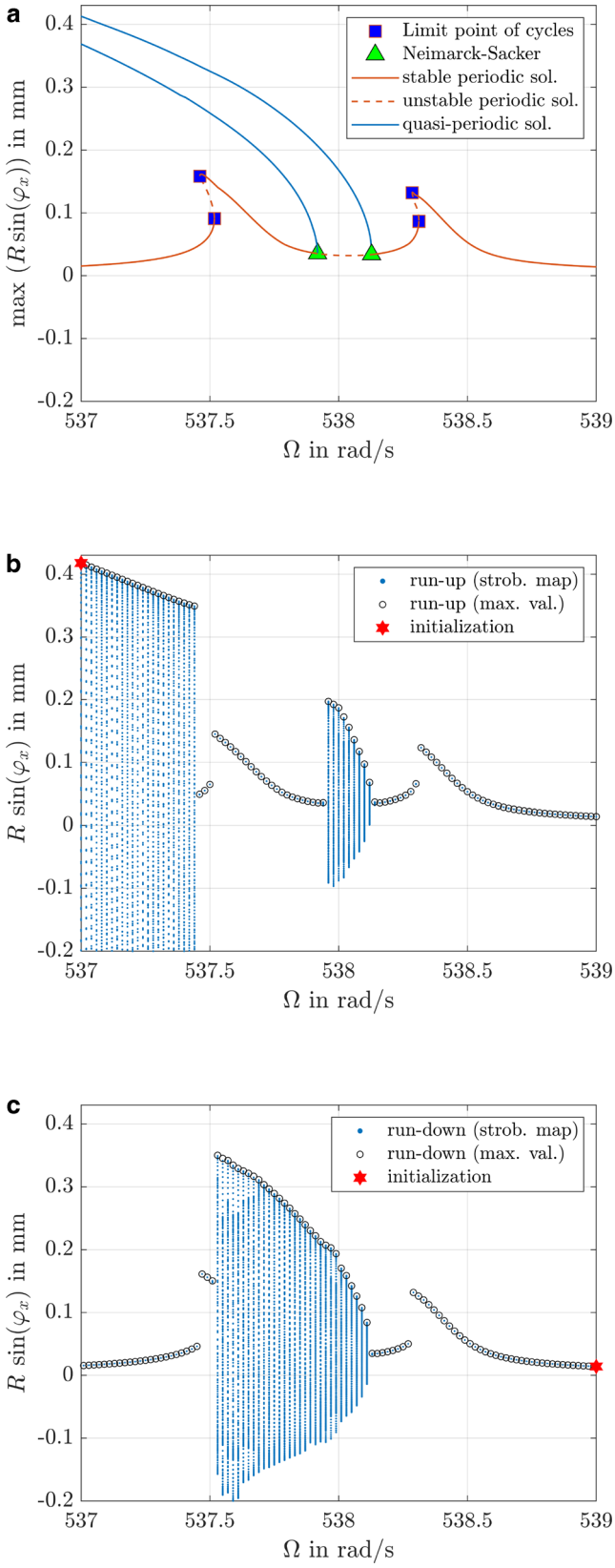


**Fig. 7** Stationary solutions in the operating range $\Omega \in [537, 539]$ rad/s for $k_{ax} = 11$: **a** Bifurcation diagram from Fourier methods, **b**,**c** Stroboscopic map with $m = 200$ points per angular velocity during run-up/run-down

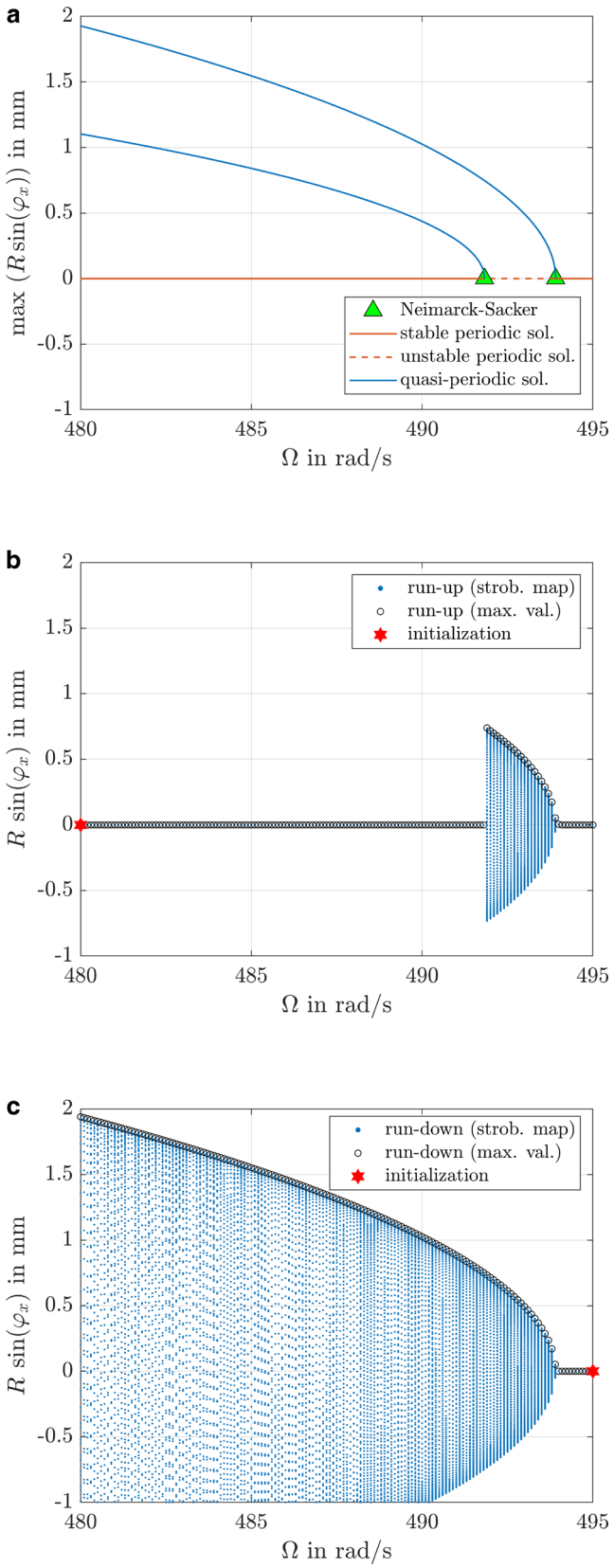


**Fig. 8** Stationary solutions in the operating range $\Omega \in [480, 495]$ rad/s for $k_{ax} = 11$: **a** Bifurcation diagram from Fourier methods, **b/c** Stroboscopic map with $m = 200$ points per angular velocity during run-up/run-down

with a smaller amplitude, which only becomes unstable in the range $\Omega \approx 493$ rad/s.

## 6 Conclusion

This publication considers the vibration behavior of the rotor disk in an axial flux switched reluctance machine under the influence of external axial excitation. A minimal model for the study of tilting vibrations is proposed. The electromagnetic forces acting on the rotor are investigated for an operating point with constant angular velocity by means of a harmonic analysis. The analysis shows that the electromagnetic forces reduce the stiffness in the tilting motion of the disk. Furthermore, they lead to non-linear softening behavior and parametric excitation in the equations of motion, with parametric excitation frequencies depending on the number of stator poles and the axial excitation frequency.

The stationary solutions show periodic and quasi-periodic behavior due to different excitation mechanisms. Thus, a procedure is described to initialize the continuation of quasi-periodic solutions by Fourier methods. The subsequent numerical analysis reveals potentially critical operating ranges with increased vibration amplitudes. The areas with increased amplitudes are described by several conditions in which an externally forced resonance or a fundamental parametric combination resonance of the system is present. Furthermore, it can be seen that a run-down of the machine can lead to critical behavior because the non-linear softening behavior of the electromagnetic forces can result in a run-down on a solution branch of high amplitudes.

## 7 Future work

In the future, the dynamics of disk-shaped rotors will be investigated experimentally. For this purpose, an existing test rig [4] was extended to include further types of excitation. Fig. 9 shows the flange of the test rig, which is excited multi-dimensionally by the electric machine behind it, the axial electromagnetic actuator and a radially acting hydraulic actuator. In addition to this torsional, axial, and radial excitation of a flange-mounted test specimen, it should also be possible in future to achieve axial excitation on the circumference of a disk-shaped test specimen. This excitation should correspond to the emulation of electromagnetic forces in the air gap. In this way, the rotor of an axial flux machine can be examined as a subsystem under the influence of various types of excitation present in electric drives. The test rig will also be used to validate the simulation results shown in this publication.

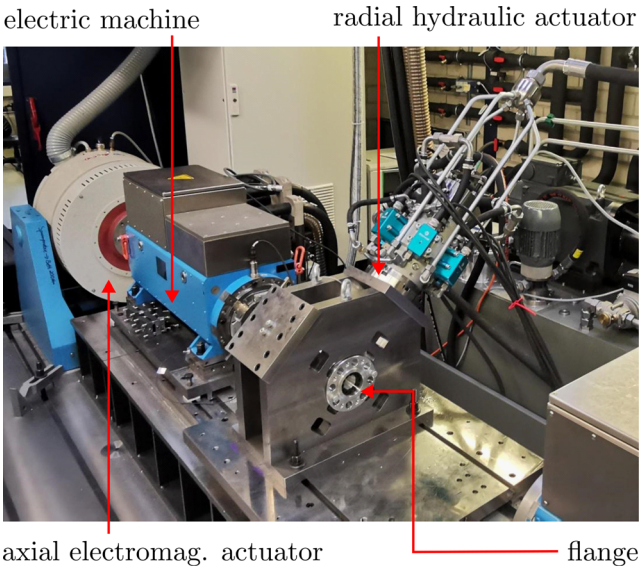


**Fig. 9** Test rig for multi-dimensional excitation of disk-shaped test specimen

**Acknowledgements** The authors are grateful for the financial support of the German Research Foundation (DFG), grant DFG_INST 121384/249-1.

**Funding** Open Access funding enabled and organized by Projekt DEAL.

**Conflict of interest** On behalf of all authors, the corresponding author states that there is no conflict of interest.

**Open Access** Dieser Artikel wird unter der Creative Commons Namensnennung 4.0 International Lizenz veröffentlicht, welche die Nutzung, Vervielfältigung, Bearbeitung, Verbreitung und Wiedergabe in jeglichem Medium und Format erlaubt, sofern Sie den/die ursprünglichen Autor(en) und die Quelle ordnungsgemäß nennen, einen Link zur Creative Commons Lizenz beifügen und angeben, ob Änderungen vorgenommen wurden. Die in diesem Artikel enthaltenen Bilder und sonstiges Drittmaterial unterliegen ebenfalls der genannten Creative Commons Lizenz, sofern sich aus der Abbildungslegende nichts anderes ergibt. Sofern das betreffende Material nicht unter der genannten Creative Commons Lizenz steht und die betreffende Handlung nicht nach gesetzlichen Vorschriften erlaubt ist, ist für die oben aufgeführten Weiterverwendungen des Materials die Einwilligung des jeweiligen Rechteinhabers einzuholen. Weitere Details zur Lizenz entnehmen Sie bitte der Lizenzinformation auf http://creativecommons.org/licenses/by/4.0/deed.de.

## References

1. Altoé P, Römer U J (2023) Fidlin Schwingungen, Rotordynamik in Axialfluss-Reluktanzmaschinen unter dem Einfluss externer Schwingungsanregung. VDI Verlag 155–170
2. Aydoun R, Parent G, Tounzi M, Lecointe JP, Komeza K (2019) Comparison of 8/6 radial and axial flux switched reluctance machines. Compel - Int J Comput Math Electr Electron Eng 38(6):1756–1769
3. Bäuerle S, Fiedler R, Hetzler H (2022) An engineering perspective on the numerics of quasi-periodic oscillations. Nonlinear Dyn 108(4):3927–3950
4. Berger J, Theuerkauf R, Ott S (2018) Neue Prüf(-stands)-Konzepte ermöglichen Validierung mehrdimensional angeregter Triebstrangteilsysteme. 19. VDI-Kongress SIMVEC - Simulation und Erprobung in der Fahrzeugentwicklung: Baden-Baden, 20. und 21.November 2018
5. Binder A (2014) Elektrische Maschinen und Antriebe: Grundlagen, Betriebsverhalten. Springer, Berlin, Heidelberg
6. Cai W, Wu X, Zhou M, Liang Y, Wang Y (2021) Review and Development of Electric Motor Systems and Electric Powertrains for New Energy Vehicles. Automot Innov 4(1):3–22
7. Cao Z, Mahmoudi A, Kahourzade S, Soong WL, Summers JR (2020) A Comparative Study of Axial-Flux versus Radial-Flux Induction Machines. In: 2020 IEEE International Conference on Power Electronics, Drives and Energy Systems (PEDES), pp 1–6
8. Dhooge A, Govaerts W, Kuznetsov YA, Meijer HG, Sautois B (2008) New features of the software MatCont for bifurcation analysis of dynamical systems. Math Comput Model Dyn Syst 14(2):147–175
9. EU Grant agreement (2016) Final Report Summary - VENUS (Switched/Synchronous Reluctance Magnet-free Motors for Electric Vehicles). Tech. rep., ID: 605429
10. Hochlenert D, Spelsberg-Korspeter G, Hagedorn P (2006) Friction Induced Vibrations in Moving Continua and Their Application to Brake Squeal. J Appl Mech 74(3):542–549
11. Huang S, Luo J, Leonardi F, Lipo T (1998) A general approach to sizing and power density equations for comparison of electrical machines. IEEE Trans on Ind Applicat 34(1):92–97
12. Huang S, Luo J, Leonardi F, Lipo T (1999) A comparison of power density for axial flux machines based on general purpose sizing equations. Ieee Trans Energy Convers 14(2):185–192
13. Husain I, Ozpineci B, Islam MS, Gurpinar E, Su GJ, Yu W, Chowdhury S, Xue L, Rahman D, Sahu R (2021) Electric Drive Technology Trends, Challenges, and Opportunities for Future Electric Vehicles. Proc Ieee 109:1039–1059
14. International Energy Agency (2015) Energy efficiency roadmap for electric motor and motor systems. Tech. rep., 4E Energy Efficient End-use Equipment
15. Krack M, Gross J (2019) Harmonic Balance for Nonlinear Vibration Problems. Mathematical Engineering. Springer, Cham
16. Kuznetsov YA (2004) Elements of Applied Bifurcation Theory, *Applied Mathematical Sciences* vol 112. Springer, New York, NY
17. Labak A, Kar NC (2013) Designing and Prototyping a Novel Five-Phase Pancake-Shaped Axial-Flux SRM for Electric Vehicle Application Through Dynamic FEA Incorporating Flux-Tube Modeling. IEEE Trans on Ind Applicat 49(3):1276–1288
18. Li S, Zhang S, Habetler TG, Harley RG (2019) Modeling, Design Optimization, and Applications of Switched Reluctance Machines—A Review. IEEE Trans on Ind Applicat 55(3):2660–2681
19. Marx B, Vogt W (2011) Dynamische Systeme. Spektrum Akademischer Verlag, Heidelberg
20. Nikolić M, Ivanović M, Terzić M, Ristić L, v. Pavlović D, Bjelić M (2022) Modal Analysis and Sound Field Modeling of a Permanent Magnet Axial Flux Machine with One Stator and Two Rotors. In: 2022 7th International Conference on Environment Friendly Energies and Applications (EFEA), pp 1–6 (ISSN: 2688-2558)
21. Parviainen A (2005) Design of axial-flux permanent-magnet low-speed machines and performance comparison between radial-flux and axial-flux machines. Ph.D. thesis (ISBN: 9789522140302)
22. Pop AA, Radulescu M, Balan H, Kanchev H (2013) Electromagnetic torque capabilities of axial-flux and radial-flux permanent-magnet machines. In: 2013 4th International Symposium on Electrical and Electronics Engineering (ISEEE), pp 1–4
23. Rajashekara K (2013) Present Status and Future Trends in Electric Vehicle Propulsion Technologies. IEEE J Emerg Sel Topics Power Electron 1(1):3–10

24. Schäfer H (ed) (2019) Elektrische Antriebstechnologie für Hybrid- und Elektrofahrzeuge. Haus der Technik Fachbuch, vol 149. expert, Tübingen
25. Schilder F, Vogt W, Schreiber S, Osinga HM (2006) Fourier methods for quasi-periodic oscillations. Numerical Meth Engineering 67(5):629–671
26. Torkaman H, Ghaheri A, Keyhani A (2019) Axial flux switched reluctance machines: a comprehensive review of design and topologies. Iet Electr Power Appl 13(3):310–321
27. Zhang B, Epskamp T, Doppelbauer M, Gregor M (2014) A comparison of the transverse, axial and radial flux PM synchronous motors for electric vehicle. In: 2014 IEEE International Electric Vehicle Conference (IEVC), pp 1–6
28. Zhang B, Seidler T, Dierken R, Doppelbauer M (2016) Development of a Yokeless and Segmented Armature Axial Flux Machine. Ieee Trans Ind Electron 63(4):2062–2071

**Publisher's Note** Springer Nature remains neutral with regard to jurisdictional claims in published maps and institutional affiliations.